Temporal solitons in air

A. A. Voronin and A. M. Zheltikov

Phys. Rev. A **95**, 023826 — Published 14 February 2017

DOI: 10.1103/PhysRevA.95.023826

Temporal solitons in air

A.A. Voronin[1,2] and A.M. Zheltikov[1,2,3,*]

[1] Physics Department, International Laser Center, M.V. Lomonosov Moscow State University, Moscow 119992, Russia

[2] Russian Quantum Center, ul. Novaya 100, Skolkovo, Moscow Region, 143025 Russia

[3] Department of Physics and Astronomy, Texas A&M University, College Station TX 77843, USA

Analysis of the group-velocity dispersion (GVD) of atmospheric air with a model that includes the entire manifold of infrared transitions in air reveals a remarkably broad and continuous anomalous-GVD region in the high-frequency wing of the carbon dioxide rovibrational band, from approximately 3.5 to 4.2 μm, where atmospheric air is still highly transparent and where high-peak-power sources of ultrashort mid-infrared pulses are available. Within this range, anomalous dispersion acting jointly with optical nonlinearity of atmospheric air is shown to give rise to a unique three-dimensional dynamics, with well-resolved soliton features in the time domain, enabling a highly efficient whole-beam soliton self-compression of such pulses to few-cycle pulse widths.

INTRODUCTION

Among a vast variety of ultrafast phenomena found in the complex spatiotemporal nonlinear dynamics of high-intensity laser fields, physical scenarios whereby spatially and temporally confined high-peak-power solitary field waveforms can be isolated are of special interest for nonlinear optical physics and ultrafast photonic technologies. As an important example, light bullet formation [1, 2] stands out as a generic scenario where nonlinear dynamics gives rise to solitary lightwaves localized in space and time. When the laser field intensity is high enough to generate free charge carriers in a nonlinear medium through ultrafast photoionization, laser-induced filamentation [3, 4] provides a universal scenario of nonlinear dynamics where beam divergence due to diffraction is suppressed due to dynamic self-action effects and field waveform confinement in the time domain is possible in certain regimes, leading to filamentation-assisted pulse compression [5, 6]. Outside the parameter space of laser filamentation, nonlinear spatiotemporal dynamics involving spatial and temporal localization

of ultrashort field waveforms has been shown to enable pulse self-compression through adiabatic pulse self-steepening within long propagation paths [7], as well as pulse compression to subcycle pulse widths in carefully designed stacks of solid materials with suitable dispersion properties [8].

In anomalously dispersive solids, spatial localization provided by spatial self-action and laser filamentation can be combined with temporal field confinement due to a solitonic dynamics of laser pulses in the time domain [9]. For carefully optimized parameters of input laser pulses, light bullets can be generated in anomalously dispersive solids as a part of laser-induced filamentation [10, 11]. If they could be extended to atmospheric air, these concepts and methods would open new avenues for a long-distance transmission of high-peak-power laser pulses and remote sensing of the atmosphere. Such an extension, however, is anything but trivial. For Ti: sapphire laser pulses, used in the overwhelming majority of laser filamentation experiments in the atmosphere, dispersion of atmospheric air is normal, leaving no parameter space for soliton dynamics. The mid-infrared range, where efficient sources of high-peak-power ultrashort pulses are now available [12, 13], seems to offer much more promise in this regard. In this wavelength region, rovibrational molecular modes within and near atmospheric absorption bands give rise to rapidly varying, sign-altering group-velocity dispersion (GVD), creating expectations that some of the minibands where the air GVD is anomalous would be broad enough to support soliton dynamics of ultrashort mid-infrared field waveforms.

An accurate analysis of GVD of atmospheric air in the mid-infrared is central for a correct identification of wavelength ranges where solitonic effects are possible. Because of a complex behavior of air refractivity within molecular absorption bands and in the wings of these bands [14], such an analysis is difficult both conceptually and technically. With full calculations of air refractivity using the high-resolution transmission molecular absorption (HITRAN) database of infrared line transitions [15] being time- and labor-consuming, a useful polynomial-fit approximation has been developed [16] to facilitate such calculations, providing a reasonable accuracy of refractive-index calculations for atmospheric air within a broad spectral range. As an important step toward finding an adequate model for the air GVD, this polynomial-fit approximation has been applied to GVD calculations, predicting an anomalous GVD of air within the range of wavelengths from approximately 3.0 to 3.3 μm [17]. Numerical simulations suggest [18, 19] that, had this anomalous-GVD region existed, generation of ultrashort mid-infrared light bullets in air would have been possible within this spectral range.

Here, we revisit the air GVD in the mid-infrared range using the full model of air refractivity including the entire HITRAN-database manifold of infrared transitions. We show that, while the polynomial-fit model provides a useful tool for approximate calculations of air dispersion within a remarkably broad spectral range, the accuracy of this approximation is inevitably limited, especially when it is extended beyond refractive-index calculations and employed for GVD analysis. As a result of unavoidable approximation errors, the mid-infrared GVD profile calculated using the full model of air refractivity deviates from GVD calculations based on the polynomial-fit approximation. The most drastic deviations are observed within the regions where radiation is resonantly coupled to molecular modes. As one of the most dramatic findings, full-air-refractivity-model calculations do not confirm the existence of continuous anomalous GVD of air within the 3.0 – 3.3-μm region, predicted by the polynomial-fit model. Instead, full-model calculations suggest that such a continuously anomalous GVD occurs within a reasonable broad spectral range in the high-frequency wing of the carbon dioxide rovibrational band, from approximately 3.5 to 4.2 μm, where atmospheric air is still highly transparent. Our numerical analysis of spatiotemporal field evolution within this wavelength range reveals physical scenarios that provide a long-distance temporal-soliton transmission of subterawatt ultrashort pulses and enable highly efficient whole-beam self-compression of such pulses to few-cycle pulse widths.

GROUP-VELOCITY DISPERSION OF AIR

For an accurate analysis of the dispersion of atmospheric air, we calculate the refractive index of atmospheric air as [14]

$$n(\omega) \approx 1 + \frac{e^2}{2m_e\varepsilon_0}\sum_k N_k \sum_i \frac{f_{ik}(\omega_{ik})}{2\omega_{0ik}}\left(\frac{1}{\omega+\omega_{0ik}-\frac{i}{2}\Gamma_{ik}} - \frac{1}{\omega-\omega_{0ik}-\frac{i}{2}\Gamma_{ik}}\right) + n_{vis}(\omega), \qquad (1)$$

Here, N_k is the density of molecules of sort k, ω_{ik}, Γ_{ik}, f_{ik} are the frequency, the linewidth, and the oscillator strength of the ith resonance in the spectrum of molecules of sort k, m_e and e are the electron mass and charge, ε_0 is the dielectric permittivity of vacuum, and $n_{vis}(\omega)$ is the refractive index of air in the visible–near-infrared range, calculated with the standard formula [20 – 22] $n_{vis}(\lambda) = B_1\left(C_1 - \lambda^{-2}\right)^{-1} + B_2\left(C_2 - \lambda^{-2}\right)^{-1}$, with $B_1 = 0.05792105$ μm^{-2}, $B_2 = 0.00167917$ μm^{-2}, $C_1 = 238.0185$ μm^{-2}, $C_2 = 57.362$ μm^{-2} [23].

In the full model of air refractivity, we calculate the refractive index of air with Eq. (1) including the entire HITRAN-database manifold of molecular transitions in air [15]. The GVD of atmospheric air can then be found as $\beta_2 = \partial^2 k/\partial\omega^2$, k and ω being the wave number and the frequency entering the dispersion relation $k(\omega)$, calculated with the use of Eq. (1) as a function of the wavelength.

With each molecular band in atmospheric absorption consisting of a large number of individual rovibrational transition lines, the refractivity of air displays rapid oscillations (Figs. 1a, 1b) within and near molecular absorption bands (Fig. 1c). In Fig. 1a, we compare predictions of the polynomial-fit model of air refractivity [16] with the results of full-model calculations that include the entire HITRAN-database manifold of infrared transitions in air [15]. As an important result, Fig. 1a helps appreciate how powerful the polynomial-fit approximation is when applied to refractive-index calculations. The refractive index of air calculated with the use of this model is seen to reproduce, with an adequate accuracy, the results of full-model calculation within a remarkably broad range of wavelengths from the visible to the long-wavelength infrared. However, GVD calculation is a very different matter as the polynomial-fit model is simply not designed to include the fine details of the dispersion profile related to individual molecular transitions within rovibrational bands. These features may be almost invisible in the refractive index (Fig. 1a), but show up in a very prominent way, upon differentiation, in the GVD (Fig. 1d), giving rise to dramatic discrepancies between the GVD profiles calculated using the full and polynomial-fit models (cf. blue solid and magenta dashed lines in Fig. 1d). Furthermore, a blow-up of the refractive index profile in Fig. 1b visualizes small-amplitude oscillations of the polynomial fit (magenta dashed line in Fig. 1b) relative to full-model calculations (blue solid line in Fig. 1b). These oscillations are, of course, typical of any polynomial fitting procedure. One of such oscillatory features (dashed circle in Fig. 1b) translates into a 3.0 – 3.3-μm anomalous-GVD artifact (dashed circle in Fig. 1d). When plugged into a pulse-evolution model, this artifact gives rise to solitonic effects, including light bullets generation [18, 19]. However, the full-air-refractivity-model prediction for the GVD β_2 within this wavelength region is very different (Fig. 1d). It suggests a rapidly varying GVD profile with multiple β_2 sign reversals – a GVD behavior that does not support any solitonic effects or light bullets on the femtosecond time scale.

Still, a full-model analysis suggests that the dispersion of air does offer a parameter space for ultrashort solitons and related solitonic phenomena. As can be seen in Fig. 1d, full-model calculations reveal a remarkably broad and continuous region of anomalous GVD that

covers a range of wavelengths from approximately 3.5 to 4.2 μm in the high-frequency wing of the CO_2 rovibrational band. Although this wavelength range is close to the CO_2 absorption band, atmospheric air is still highly transparent in the central part of this anomalous-GVD region, with the absorption length of 3.9-μm radiation estimated as $l_a \approx 40$ km. For comparison, the absorption length at the center of the CO_2 absorption band, at $\lambda = 4.26$ μm, is only $l_a \approx 1$ m. The bandwidth of this region is broad enough to support temporal solitons as short as ~200 – 250 fs (assuming the central wavelength $\lambda \approx 3.9$ μm), although perturbations due to high-order dispersion are inevitable, especially near the CO_2 absorption band edge (Fig. 1d). As a stroke of luck, the central wavelength of high-peak-power OPCPA sources capable of generating such short pulses in the mid-infrared [12, 13], $\lambda \approx 3.9$ μm, falls right into this wavelength range, promising practical technologies for long-distance transmission of subterawatt and terawatt mid-infrared pulses and pulse compression based on solitonic effects in atmospheric air.

MODEL OF SPATIOTEMPORAL FIELD EVOLUTION

Our numerical analysis of spatiotemporal field evolution in atmospheric air is based on the three-dimensional time-dependent generalized nonlinear Schrödinger equation (GNSE) [3, 4, 24, 25] for the complex amplitude of the field, which is referred to hereinafter as the GNSE model,

$$\frac{\partial}{\partial z}\tilde{A} = \left[\frac{ic}{2\omega n_0}\Delta_\perp + i\tilde{D}(\omega)\right]\tilde{A} + \tilde{F}\left[i\frac{\omega_0\tilde{T}}{c}\left[n_2(1-f_R)|A|^2 + f_R\int_0^\infty R(\eta')|A(\eta-\eta')|^2 d\eta' + n_4|A|^4\right]A - \frac{U_i W(I)(\rho_0-\rho(\eta))}{2I}A\right] - \left(\frac{i\omega_0^2\omega}{2cn_0\rho_c(\omega^2+\tau_c^{-2})} + \frac{\sigma(\omega)}{2}\right)\tilde{F}[\rho(\eta)A] \quad (2)$$

Here, $A \equiv A(\eta,x,y,z)$ is the field envelope, $\tilde{A} \equiv \tilde{A}(\omega,x,y,z)$ is its Fourier transform, x, y are the transverse coordinates, z is the coordinate along the propagation axis, η is the retarded time, $\omega = 2\pi c/\lambda$ is the radiation frequency, λ is the wavelength, $\tilde{F}$ is the Fourier transform operator, $\Delta_\perp = \partial^2/\partial x^2 + \partial^2/\partial y^2$ is the diffraction operator, $\tilde{D} = k(\omega) - k(\omega_0) - \partial k/\partial\omega|_{\omega 0}(\omega - \omega_0)$ is the dispersion operator, ω_0 is the central frequency, $k(\omega) = \omega n(\omega)/c$, $n(\omega)$ is the refractive index, $n_0 = n(\omega_0)$, n_2 and n_4 are the Kerr nonlinearity coefficients, $\tilde{T} = 1 + i\omega_0^{-1}\partial/\partial\eta$, $R(\eta)$ is the delayed nonlinear response, $\rho \equiv \rho(\eta,x,y,z)$ is the electron density, ρ_0 is the neutral gas density, $\rho_c = \omega_0^2 m_e\varepsilon_0/e^2$ is the critical electron density, $U_i = U_0 + U_{osc}$, U_i is the ionization potential, U_{osc} is the energy of field-induced electron oscillations, $W(I)$ is the photoionization

rate, I is the field intensity, $\sigma(\omega)$ is the impact ionization cross section, and e and m_e are the electron charge and mass, respectively.

The field evolution equation [Eq. (2)] is solved jointly with the rate equation for the electron density, $\partial\rho/\partial t = W + \sigma(\omega_0)U_i^{-1}\rho I$, which includes impact ionization and photoionization with the photoionization rate W calculated using the Keldysh formalism [26]. When supplemented with this equation for ρ, our GNSE-based model includes all the key physical phenomena that have been identified as significant factors behind a truly three-dimensional spatiotemporal evolution of ultrashort optical pulses in nonlinear media, such as dispersion and absorption of the medium, beam diffraction, Kerr and Raman nonlinearities, pulse self-steepening, spatial self-action phenomena, as well as ionization-induced loss, dispersion, and optical nonlinearities.

The way the dispersion of atmospheric air is included in Eq. (2) is, perhaps, the most significant distinctive feature of our approach. Since our main focus here is to identify negative-dispersion and, in particular, solitonic phenomena in the dynamics of ultrashort laser pulses in air, dispersion of the atmosphere needs to be included into our model as accurately as possible. The frequency-domain representation of the dispersion operator $\tilde{D}$ is ideally suited to achieve this goal. Indeed, there is simply no way that the standard time-domain approach using a polynomial expansion of $k(\omega)$ about ω_0 with constant dispersion coefficients could be possibly tailored to describe the realistic dispersion profile of atmospheric air in its entire complexity as defined by modern databases, such as the HITRAN database. By contrast, when written in the frequency domain, the dispersion operator can be defined in such a way as to accommodate all the fine details of atmospheric dispersion in the spectral domain of interest that influence the dynamics of optical field waveforms on the subpicosecond time scale. In simulations presented below in this paper, the $\tilde{D}$ operator was programmed to include all the pertinent features of air refractivity from the HITRAN database [15] related to the asymmetric-stretch rovibrational band of atmospheric CO_2 (with a density $N_{CO2} = 10^{16}$ см$^{-3}$), as well as all the rovibrational bands of water ($N_{H2O} = 5.4\ 10^{16}$ см$^{-3}$) falling within the range from 1.8 to 4.5 μm (Figs. 1b, 1d). Although individual rovibrational components within these bands appear almost as discontinuities in Figs. 1a – 1d, their linewidths [Γ_{ik} in Eq. (1)] are finite and are typically of the order of $\Gamma_{ik}/(2\pi) \sim 2$ GHz for the asymmetric-stretch rovibrational band of atmospheric CO_2 [27, 28].

Simulations are performed for typical parameters of the atmospheric air – the ionization potential molecular oxygen $U_i = 12.063$ eV and the Raman function $R(\eta) = (\tau_1^2 + \tau_2^2)\tau_1^{-1}\tau_2^{-2}\exp(-\eta/\tau_2)\sin(\eta/\tau_1)$, with $f_R = 0.5$, $\tau_1 = 62.5$ fs, $\tau_2 = 70$ fs [3, 4, 29]. The Kerr-effect nonlinear

refractive index coefficients n_2 and n_4 have never been accurately characterized in this wavelength range. In simulations presented here, we use the n_2 and n_4 coefficients, $n_2 \approx 2.8 \cdot 10^{-19}$ cm^2/W, $n_4 \approx -1 \cdot 10^{-33}$ cm^4/W^2, that provide the best fit simultaneously for the spectra, pulse shapes, and beam profiles measured for ultrashort 3.9-μm laser pulses transmitted through atmospheric air [13, 30, 31].

The field evolution equation (2) is solved by the split-step method. The linear diffraction and dispersion operators in this equation are computed using the Fourier method. The nonlinear part of the field evolution equation, as well as the equation for the electron density dynamics are solved by the fifth-order Runge–Kutta method. Simulations are performed using an MPI parallel programming interface and the CUDA graphical architecture on the Lomonosov and Lomonosov-2 supercomputer clusters of Moscow State University (see Refs. 32, 33 for the details of parallel algorithms and optimization of computer resources).

In freely propagating laser beams, soliton dynamics occurs as a part of complex spatiotemporal field evolution. In this regime, soliton field transformations in the time domain are often strongly coupled to nonlinear beam dynamics. As a result, canonical soliton effects known from textbook nonlinear fiber optics are very rarely observed in their pure form. Still, with a careful choice of input laser parameters, a decrease in the field intensity due to diffraction-induced beam divergence can be significantly reduced by self-focusing. In this regime, the soliton effects, as we will show below, can be decoupled from beam dynamics, helping isolate soliton phenomena in three-dimensional field evolution in freely propagating laser beams.

RESULTS AND DISCUSSION

Envisaging experiments with mid-infrared OPCPA sources [12, 13] as, perhaps, the most realistic option for nearest-future experimental studies of solitonic effects in atmospheric air, we examine the spatiotemporal evolution of laser pulses in a nonfocused beam with a central wavelength $\lambda_0 = 3.9$ μm, an input pulse width $\tau_0 = 250$ fs, and an initial pulse energy $W_0 = 25$ mJ. The input peak power, $P_0 = 100$ GW, is adjusted to be right above the critical power of self-focusing, $P_{cr} \approx 80$ GW at $\lambda_0 = 3.9$ μm, which, along with the choice of the input beam diameter, $d_0 = 14$ mm, helps reduce diffraction beam divergence, avoiding, at the same time, filamentation of the laser beam (Fig. 2a) and any noticeable photoionization of air.

In Fig. 2a, along with the map of overall beam dynamics, we present the effective mean beam radius, defined as

$$r_b(z)=\left(\int_0^{\infty}\left(\int_{-\infty}^{\infty}I(z,r,\eta)d\eta\right)2\pi r^3dr\right)^{1/2}\left(\int_0^{\infty}\left(\int_{-\infty}^{\infty}I(z,r,\eta)d\eta\right)2\pi rdr\right)^{-1/2}, \quad (3)$$

where r is the radial coordinate and the field intensity $I(z, r, \eta)$ is found by solving the 3d field evolution equation (2). In Fig. 2a, we compare the behavior of r_b as a function of z calculated using the full 3d spatiotemporal model of Eq. (2) (solid line) with the $r_b(z)$ dependence calculated with the self-action term in the 3d GNSE disabled (dashed line). Comparison of these $r_b(z)$ dependences gives a quantitative measure of diffraction beam divergence suppression due to self-focusing. As can be seen from Fig. 2a, self-focusing prevents rapid beam divergence, helping sustain high field intensities, needed for soliton dynamics, within much longer propagation paths.

A laser pulse with such input parameters becomes shorter (Figs. 2b, 2c) as it propagates through atmospheric air within the anomalous-GVD range, attaining a pulse width of about 80 fs at $z_m \approx 90$ m (Fig. 2c). Integration over the entire beam at this point yields a pulse with a pulse width $\tau_m \approx 105$ fs (Fig. 2b). To identify solitonic effects in this pulse self-compression dynamics, in Figs. 2c and 2d, we compare simulations performed by solving the 3d GNSE [Eq. (2)] with the solution of the 1d GNSE [34] for a laser pulse with the same input parameters (Figs. 2e, 2f). The 1d GNSE model is instrumental here as it fully ignores diffraction and spatial self-action effects, but can accurately describe the 1d temporal soliton dynamics in the presence of high-order dispersion, which tends to grow in its significance near the CO_2 absorption band edge (Fig. 1b).

The 3d dynamics of a freely propagating laser beam is seen to closely follow the 1d evolution of a laser pulse, exhibiting clear signatures of soliton self-compression (Figs. 2c, 2e), as well as spectral broadening dominated by self-phase modulation (Figs. 2d, 2f). Moreover, even a quantitative comparison of 1d and 3d scenarios is meaningful in this regime. Indeed, while in 3d dynamics, the minimum on-axis pulse width $\tau_m \approx 80$ fs is achieved at $z_m \approx 90$ m (Fig. 2c), the 1d GNSE dictates pulse compression to a pulse width of about 60 fs within the same optimal pulse compression length (Fig. 2e).

To demonstrate a high-efficiency soliton self-compression in atmospheric air, we consider the 3d spatiotemporal evolution of laser pulses with the same values of λ_0, τ_0, and W_0 as specified above, but with a much smaller beam diameter, $d_0 = 4.2$ mm. Since the diffraction length l_{df} for such a beam diameter is more than an order of magnitude shorter than l_{df} in Fig. 2, while the input peak power is kept unchanged, self-focusing is now too weak to suppress diffraction-induced beam divergence within a noticeable propagation path (Fig. 3a). In this

regime, temporal transformations of laser pulses are coupled to beam dynamics, and any 1d model is no longer accurate.

However, the field intensity in such a smaller-d_0 beam within the initial section of its propagation path (1.4 TW/cm^2 at z = 0 m in Fig. 3a) is much higher than the field intensity in a laser beam shown in Fig. 2a (0.12 TW/cm^2 at z = 0 m). As a result, laser pulses in such a beam are compressed to much shorter pulse widths, becoming as short as ≈ 40 fs at $z_m \approx 42$ m on the beam axis (Fig. 3d). The spectral broadening of such pulses, dominated by self-phase modulation, tends to fill up the entire atmospheric transmission window, giving rise to sharp edges of output spectra at 2.75 and 4.2 μm and an extended tail stretching beyond the long-wavelength edge of the CO_2 absorption line (Figs. 3b, 3c).

To isolate the role of dispersion effects in the pulse-compression scenario illustrated in Figs. 2a – 2f, 1-d simulations without the dispersion and absorption terms in the 1d GNSE have been performed. In Figs. 2e – 2h, these simulations are compared with simulations using the full 1d GNSE model with the dispersion and absorption terms included. As can be seen from Figs. 2e and 2g, the difference in the temporal dynamics of laser pulses simulated with and without dispersion is striking. When the dispersion term is disabled, the pulse is seen to show no sign of self-compression whatsoever (Fig. 2g). On the other hand, when anomalous dispersion of air is included in the model, the laser pulse shortens to a pulse width of about 60 fs at $z \approx 90$ m as a part of solitonic pulse self-compression dynamics.

Unlike filamentation-assisted pulse compression, where efficient pulse shortening is often limited to a small area near the beam axis, soliton pulse compression considered in this work can be made remarkably uniform across the laser beam. Indeed, while the minimum pulse width achieved at $z_m \approx 42$ m on the beam axis is about 40 fs (Fig. 3d), integration over the entire beam at this point yields only a slightly longer pulse with a pulse width $\tau_m \approx 50$ fs (Figs. 3e, 3f) and an energy $W_m \approx 24.3$ mJ, corresponding to a compression ratio $\tau_m/\tau_0 \approx 5$ with an energy throughput as high as $W_m/W_0 \approx 96.8\%$. Defining the peak power of the compressed pulse as $P_m = \max_{\eta} \int_0^{\infty} I(r,\eta)\, 2\pi r dr$, we find $P_m \approx 200$ GW, which is twice as high as the peak power of the input pulse.

CONCLUSION

To summarize, analysis of air refractivity with a model that includes the entire manifold of infrared transitions in air suggests the existence of a remarkably broad and continuous anomalous-GVD region in the high-frequency wing of the carbon dioxide rovibrational band,

from approximately 3.5 to 4.2 μm, where atmospheric air is still highly transparent and where high-peak-power sources of ultrashort mid-infrared pulses are available. Within this range, anomalous dispersion acting jointly with optical nonlinearity of atmospheric air is shown to give rise to a unique three-dimensional dynamics, with well-resolved soliton features in the time domain, enabling a long-distance transmission of subterawatt ultrashort mid-infrared pulses and highly efficient whole-beam soliton self-compression of such pulses in the time domain to few-cycle pulse widths.

ACKNOWLEDGMENTS

This research was supported in part by the Russian Foundation for Basic Research (projects nos. 14-29-07182, 16-02-00843, 16-32-60164, and 15-32-20713), the Russian Science Foundation (project no. 14-12-00772), the Welch Foundation (Grant No. A-1801), and ONR (Award No. 00014-16-1-2578).

References

1. Y. Silberberg, Opt. Lett. **15,** 1282 (1990).

2. A. L. Gaeta, in *Self-focusing: Past and Present* (Springer, Berlin, 2009), p. 399.

3. L. Berge, S. Skupin, R. Nuter, J. Kasparian, and J.-P. Wolf, Rep. Prog. Phys. **70,** 1633 (2007).

4. A. Couairon, and A. Mysyrowicz, Phys. Rep. **441,** 47 (2007).

5. C.P. Hauri, W. Kornelis, F.W. Helbing, A. Heinrich, A. Couairon, A. Mysyrowicz, J. Biegert, and U. Keller, Appl. Phys. B **79,** 673 (2004).

6. A. Couairon, M. Franco, A. Mysyrowicz, J. Biegert, and U. Keller, Opt. Lett. **30,** 2657 (2005).

7. P. A. Zhokhov and A. M. Zheltikov, Phys. Rev. Lett. **110,** 183903 (2013).

8. E.A. Stepanov, A.A. Lanin, A.A. Voronin, A.B. Fedotov, and A.M. Zheltikov, Phys. Rev. Lett. **117,** 043901 (2016).

9. M. Durand, A. Jarnac, A. Houard, Y. Liu, S. Grabielle, N. Forget, A. Durécu, A. Couairon, and A. Mysyrowicz, Phys. Rev. Lett. **110,** 115003 (2013).

10. D. Majus, G. Tamošauskas, I. Gražulevičiūtė, N. Garejev, A. Lotti, A. Couairon, D. Faccio, and A. Dubietis, Phys. Rev. Lett. **112,** 193901 (2014).

11. I. Gražulevičiūtė, G. Tamošauskas, V. Jukna, A. Couairon, D. Faccio, and A. Dubietis, Opt. Express **22,** 30613 (2014).

12. G. Andriukaitis, T. Balčiūnas, S. Ališauskas, A. Pugžlys, A. Baltuška, T. Popmintchev, M.-C. Chen, M. M. Murnane, and H. C. Kapteyn, Opt. Lett. **36,** 2755 (2011).

13. A. V. Mitrofanov, A. A. Voronin, D. A. Sidorov-Biryukov, A. Pugžlys, E. A. Stepanov, G. Andriukaitis, T. Flöry, S. Ališauskas, A. B. Fedotov, A. Baltuška, and A. M. Zheltikov, Scientific Reports **5,** 8368 (2015).

14. R.J. Mathar, Appl. Opt. **43**, 928 (2004).

15. URL: http://www.cfa.harvard.edu/hitran/.

16. R. J. Mathar, J. Opt. A, Pure Appl. Opt. **9**, 470 (2007).

17. B. Shim, S. E. Schrauth, and A. L. Gaeta, Opt. Express **19,** 9118 (2011).

18. E. O. Smetanina, V. Y. Fedorov, A. E. Dormidonov, and V. P. Kandidov, J. Phys. Conf. Ser. **541**, 012071 (2014).

19. S. V. Chekalin, A. E. Dokukina, A. E. Dormidonov, V. O. Kompanets, E. O. Smetanina, and V. P. Kandidov, J. Phys. B **48,** 094008 (2015).

20. B. Edlén, Metrologia **2**, 71 (1966).

21. E.R. Peck and K. Reeder, J. Opt. Soc. Am. **62**, 958 (1972).

22. K.P. Birch and M.J. Downs, Metrologia **30**, 155 (1993).

23. P.E. Ciddor, Appl. Opt. **35**, 1566 (1996).

24. N. Berti, W. Ettoumi, J. Kasparian, and J.-P. Wolf, Opt. Express **22**, 21061 (2014).

25. A.A. Voronin, and A.M. Zheltikov, Phys. Rev. A **4,** 043807 (2014).

26. L.V. Keldysh, Sov. Phys. JETP **20,** 1307 (1965).

27. G. Herzberg, *Molecular spectra and molecular structure: III Electronic spectra and electronic structure of polyatomic molecules* (Van Nostrand, 1966).

28. A.A. Lanin, A.A. Voronin, A.B. Fedotov, and A.M. Zheltikov, Sci. Reports **4**, 6670 (2014).

29. A.M. Zheltikov, Opt. Lett. **32**, 2052 (2007).

30. A.V. Mitrofanov, A.A. Voronin, S.I. Mitryukovskiy, D.A. Sidorov-Biryukov, A. Pugžlys, G. Andriukaitis, T. Flöry, E.A. Stepanov, A.B. Fedotov, A. Baltuška, and A.M. Zheltikov, Opt. Lett. **9,** 2068 (2015).

31. A.V. Mitrofanov, A.A. Voronin, D.A. Sidorov-Biryukov, S.I. Mitryukovsky, M.V. Rozhko, A. Pugžlys, A.B. Fedotov, V.Ya. Panchenko, A. Baltuška, A.M. Zheltikov, Opt. Lett. **41,** 3479 (2016).

32. A.A. Voronin and A.M. Zheltikov, Phys. Usp. **59** (9) (2016); DOI: 10.3367/UFNe.2016.02.037700

33. A.A. Voronin, V.Ya. Panchenko, and A.M. Zheltikov, Laser Phys. Lett. **13**, 065403 (2016).

34. G.P. Agrawal, *Nonlinear Fiber Optics* (Academic, New York, 2001).

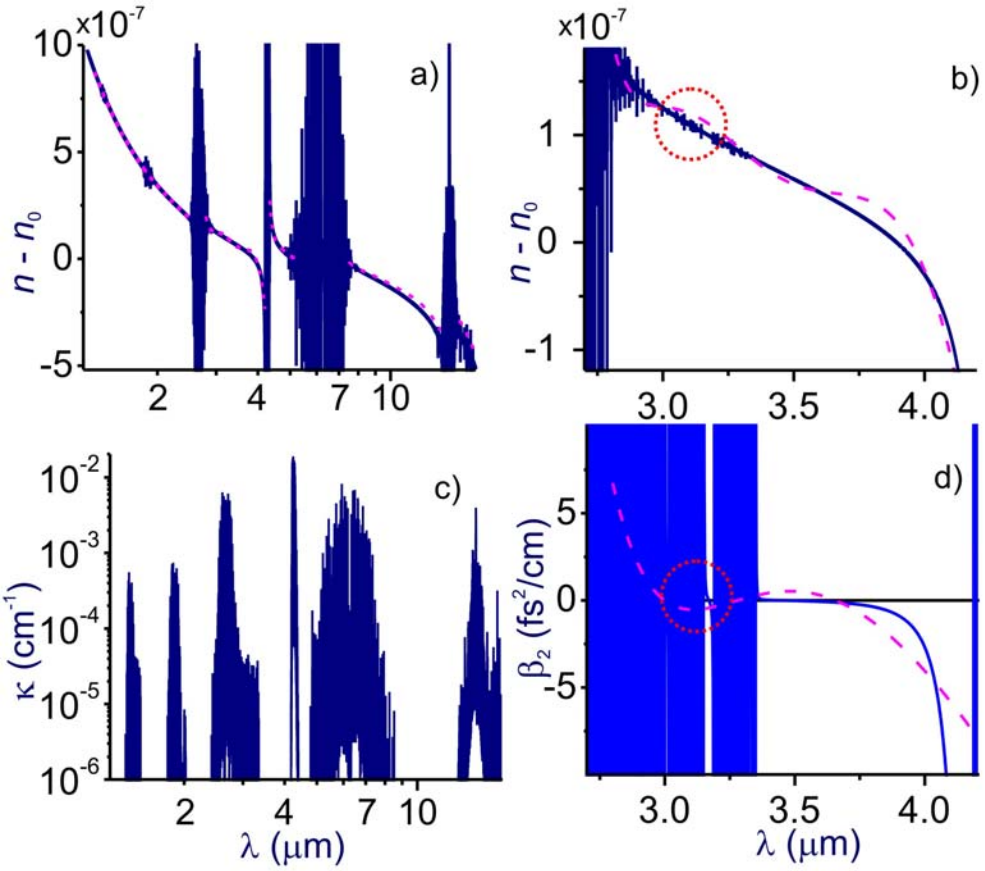

Fig. 1. (a) The refractive index of atmospheric air calculated with the full model including the entire manifold of HITRAN-database infrared transitions (blue solid line) and the polynomial-fit model (magenta dashed line). (b) Blow-up of the refractive index of atmospheric air within the 2.6 – 4.2 μm wavelength range calculated with the full model including the entire manifold of HITRAN-database infrared transitions (blue solid line) and the polynomial-fit model (magenta dashed line). (c) Absorption spectrum of atmospheric air, $\kappa(\lambda)$, calculated with the full model including the entire manifold of HITRAN-database infrared transitions. (d) Group-velocity dispersion β_2 of atmospheric air within the 2.6 – 4.2 μm wavelength range calculated with the full model including the entire manifold of HITRAN-database infrared transitions (blue solid line) and the polynomial-fit model (magenta dashed line). The 3.0 – 3.3-μm anomalous-GVD artifact is contoured by a dashed circle. Full-model calculations are performed for atmospheric air at a temperature of 17.5°C, humidity of 10%, pressure of 101325 Pa, and CO_2 content of 370 ppm; $n_0 \approx 1.000269919$ is the refractive index of air at $\lambda = 3.9$ μm.

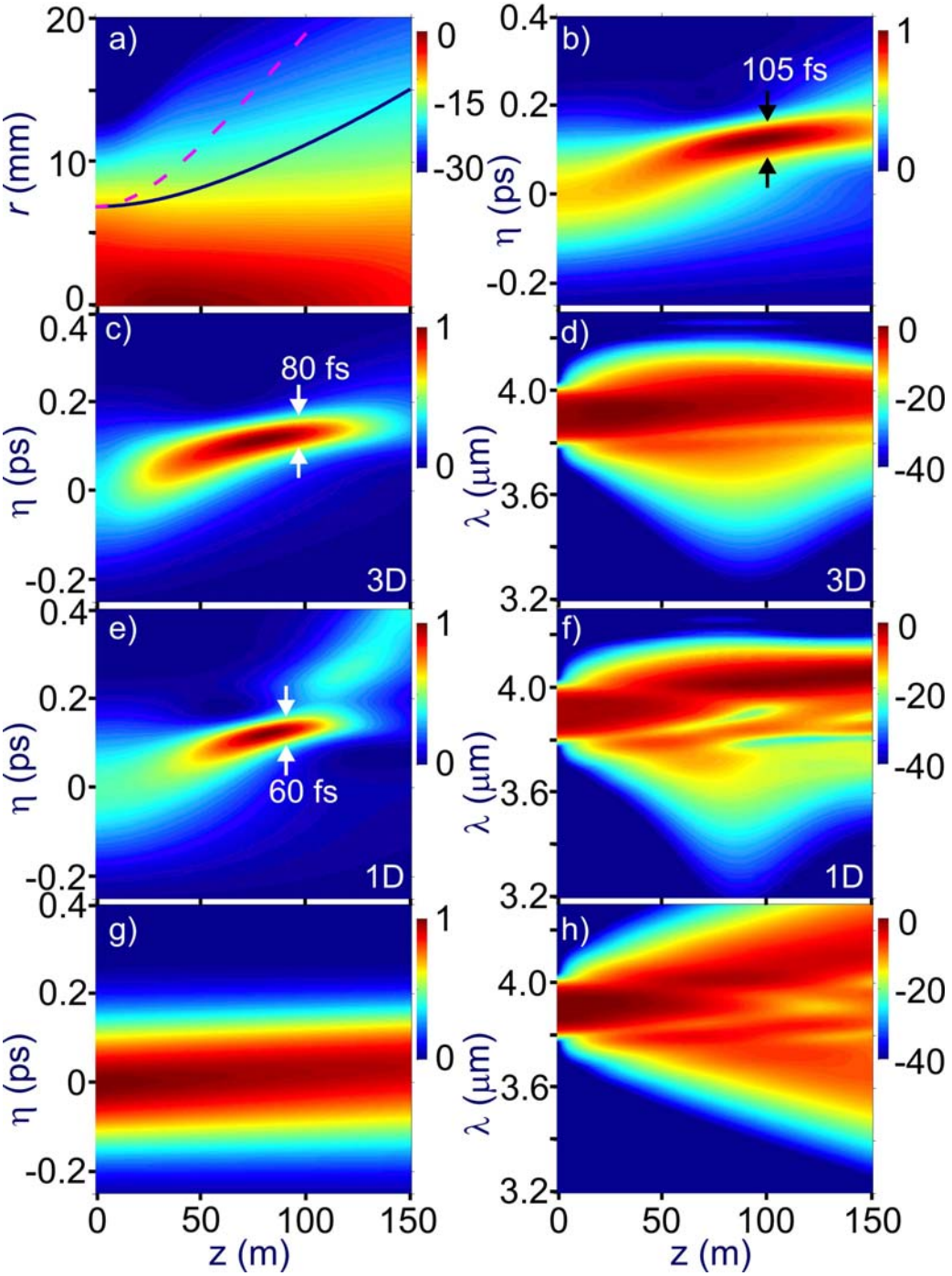

Fig. 2. Nonlinear dynamics mid-infrared pulses with $\lambda_0 = 3.9$ μm, $\tau_0 = 250$ fs, $W_0 = 25$ mJ, and $d_0 = 14$ mm in air in (3+1)-d (a – d) and (1+1)-d (e – h) simulations with (a – f) and without (g, h) dispersion and absorption: (a) beam dynamics with the beam radius r_b calculated in the full model of beam dynamics (solid line) and with self-focusing disabled (dashed line), (b) temporal evolution of the field intensity integrated over the entire beam, (c, d) temporal (c) and spectral (d) evolution of the field intensity on the beam axis, and (e – h) temporal (e, g) and spectral (f, h) evolution in 1d dynamics with (e, f) and without (g, h) dispersion and absorption.

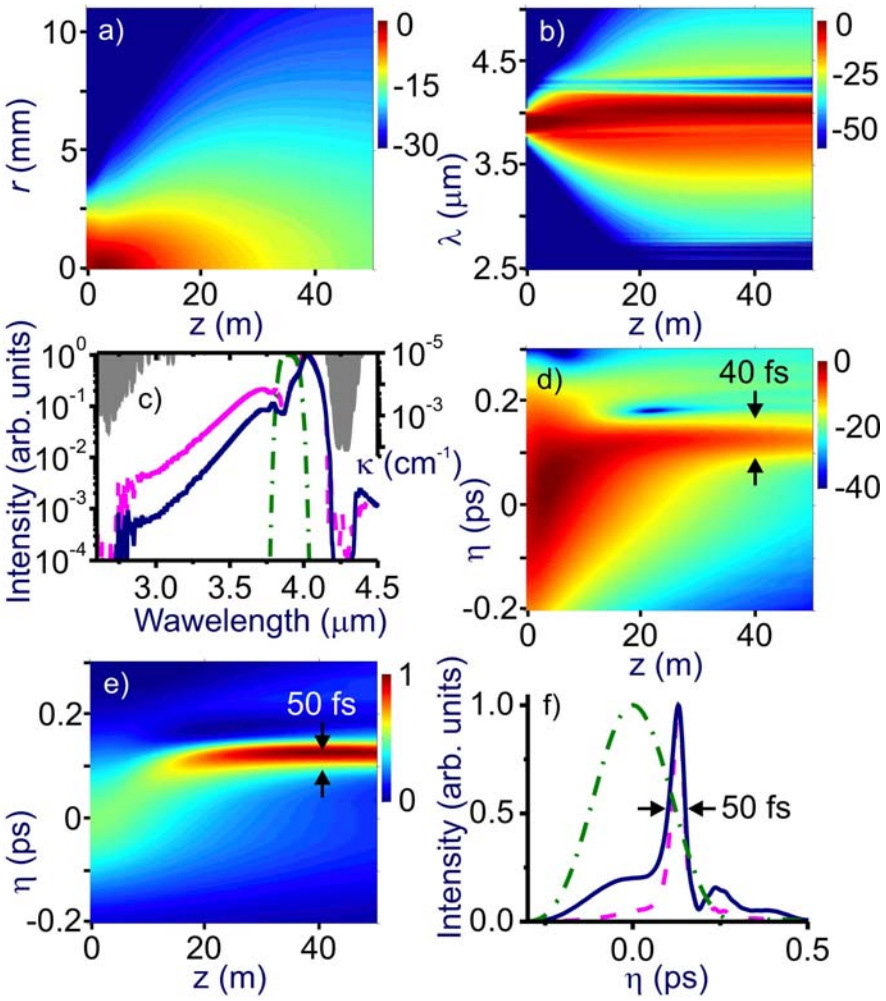

Fig. 3. Soliton self-compression of mid-infrared pulses with $\lambda_0 = 3.9$ μm, $\tau_0 = 250$ fs, $W_0 = 25$ mJ, and $d_0 = 4.2$ mm in air: (a) beam dynamics, (b) spectral evolution, (c) the spectrum at the point of maximum pulse compression, $z = 42$ m, with the absorption spectrum of air shown by grey shading, (d) temporal evolution of the field intensity on the beam axis, (e) temporal evolution of the field intensity integrated over the entire beam, and (f) temporal envelope of the mid-infrared pulse on the beam axis (dashed line) and integrated over the entire beam (solid line) at the point of maximum pulse compression, $z = 42$ m, versus the input pulse (dash–dotted) line.